Friction and wear characteristics of DLC-terminated coatings deposited on AlSi10Mg alloy produced by Additive Manufacturing

E. Salerno [a,1], D. Casotti [a,2], E. Gualtieri [b,c], A. Ballestrazzi [b,c], G.C. Gazzadi [a], G. Bolelli [b,d], L. Lusvarghi [b,d], A. Rota [a,b,c], S. Valeri [a,b,c], G. Paolicelli [a,*]

[a] *CNR-NANO Istituto Nanoscienze, Via Campi 213/a, 41125 Modena, Italy*
[b] *Centro Interdipartimentale per la Ricerca Applicata e i Servizi nella Meccanica Avanzata e nella Motoristica Intermech-Mo.Re. - Università di Modena e Reggio Emilia, Italy*
[c] *FIM – Dipartimento di Scienze Fisiche, Informatiche e Matematiche, Università di Modena e Reggio Emilia, Italy*
[d] *DIEF – Dipartimento di Ingegneria "Enzo Ferrari", Università di Modena e Reggio Emilia, Italy*

ARTICLE INFO

ABSTRACT

Al–Si alloys are attractive materials for the fabrication of mechanical components, mainly because of their high strength-to-density ratio. Though the advent of Selective Laser Melting (SLM) has potentially expanded the range of their applicability, their poor tribological performances limit their effective use. Identifying post-processing protocols and coating strategies enhancing these properties and compatible with large-scale production is fundamental to the industrial uptake of SLM-fabricated Al–Si parts. This work tests the possibility of depositing self-lubricating Diamond-Like Carbon (DLC)-terminated films on AlSi10Mg built by SLM and subjected to different surface finishing processes. The applied coating architectures consist of an electroless nickel-phosphorus buffer layer deposited on the AlSi10Mg surface, plus a series of interlayers and a DLC top film grown by Plasma Assisted – Chemical Vapor Deposition. The wear resistance and frictional behavior of the samples are evaluated for different substrate pre-treatments and coating assemblies under two applied loads. Cast substrates, processed and coated in a similar way, are also studied for comparison. The DLC film lends good tribological performances to all the coating-substrate combinations explored, being mechanically assisted by the underlying Ni–P layer. The friction coefficients stabilize around 0.20 at the lowest load, independently of the sample surface roughness (S_q), which spans the range 0.47–4.6 μm. Conversely, the counterpart wear rates increase with roughness up to 10^{-5} mm^3/(N·m). Both tribological parameters decrease by nearly 20 % and 70 %, respectively, after a tenfold increase in load. These results indicate that DLC-terminated multilayers are extremely efficient on AlSi10Mg even in the presence of significant roughness. Their application requires a limited number of well-established processing steps also in the case of SLM grown parts.

1. Introduction

Aluminum alloys keep deserving great attention in mechanical applications, and in particular in the aerospace and automotive industry. Since the 1980s, improving aircraft and vehicle fuel economy by reducing the weight of components has been a driving factor for the development and spread of lightweight materials. The low density of Al alloys, accompanied by their large strength-to-weight ratio, high thermal conductivity and good corrosion resistance made them the material

of choice in substitution of steel and cast iron [1–4]. Advances in the composition, manufacturing processes and strengthening approaches enabled Al alloys to meet high-performance requirements and to be progressively incorporated in a broad range of components, both structural and non-structural [1,4–7]. The latter category also includes engine parts in relative motion, such as engine blocks, cylinder heads and pistons, where especially Al–Si cast alloys find substantial application, even though they have poor inherent tribological performances [7–9].

The recent introduction of Additive Manufacturing (AM) techniques stimulated renewed interest in Al alloys. AM offers unprecedented design flexibility and part consolidation, implying a net saving of materials and production costs [10,11]. In addition, the manufacturing principle of additive techniques for metals, based on the layer-by-layer melting of the raw material [4], opens up new opportunities and challenges for the microstructure and mechanical properties of the final product. At present, Laser-Powder Bed Fusion (L-PBF), also known as Selective Laser Melting (SLM), is one of the AM techniques most widely used with Al alloys, having particular affinity with Al–Si alloys like AlSi10Mg and AlSi12 because of their good weldability [12,13]. Compared to conventional manufacturing methods, SLM confers a finer and more uniform microstructure to the Al–Si alloys, thanks to the rapid movement of the laser and the correspondingly fast kinetics of solidification [12,13]. In alloys near the eutectic composition (~12 wt% of Si), the slow cooling rate in the casting process results in a coarse dendritic structure with grains of several tens of microns in size, separated by acicular or lamellar eutectic Si of needle or plate shape [14–16], whose morphology affects ductility and strength [7,17]. Conversely, an ultra-fine cellular α-Al phase with average diameters down to ~500 nm, surrounded by a fibrous Si network, is distinctive of SLM Al–Si alloys resulting in improved tensile properties [12,13,17,18]. Nevertheless, the ultimate tensile strength of these materials hardly exceeds 400 MPa [4,12,13], so they are valid candidates mainly for components with low or moderate load-bearing requirements, as for example the above-mentioned engine parts, for which the tribological aspects are of great relevance.

As a consequence of the refined microstructure, as-built SLM Al–Si alloys also have greater hardness and better wear resistance than their cast equivalents [19,20]. However, reported wear rates are quite large in absolute terms, being in the order of 10^{-3}–10^{-4} mm^3/(N·m) in conjunction with friction coefficients >0.4, when measured under dry sliding conditions against hard counterparts [19–22]. Therefore, post-fabrication strategies aimed at improving these parameters need to be implemented. Diamond-Like Carbon (DLC) coatings are a well-established solution to protect metallic parts from wear damage and to cut down friction losses [23–27]. Basically consisting of carbon atoms in both sp^2 and sp^3 hybridization with possible hydrogen incorporation, DLC coatings have high hardness, self-lubricating behavior, good thermal stability within the temperature range where Al-alloys are usually employed, and chemical inertness [28–30], which make them more attractive than other protective coatings. However, the deposition of DLC films on aluminum-based substrates is challenging, as it is hindered by the large differences in hardness, elastic modulus and thermal expansion coefficient which compromise coating adhesion and performances [31]. Spontaneous detachment was observed in [32,33] for DLC films directly grown on aluminum alloys. Malaczynski et al. [34] reported partial flaking and delamination of the coating in the absence of a bonding interlayer between DLC and A390 alloy. Carbon implantation and sputter cleaning before DLC deposition improved the coating/substrate adhesion, but minimum friction coefficients around 0.4 were measured and no conclusive indications on the wear behavior could be drawn. An a-C:H-terminated multilayer film was applied in [35] to AA 6082-T6 plates. To avoid thermal alteration of the substrate and large thermal mismatch stresses, the surface activation process was kept at low energetic levels and a low deposition temperature was maintained. Early failure of the film occurred in both scratch adhesion and sliding wear tests because of cracking and spallation. More encouraging results were obtained after the interposition of a thick (75–125 μm) cermet layer: thanks to the better mechanical support, the critical cracking load increased and low values of friction coefficient (0.1–0.2) and wear rate (10^{-6}–10^{-7} mm^3/(N·m)), typical of hydrogenated DLC films in humid air [29], were achieved as long as the film did not crack. Recent studies have confirmed that properly designed multilayer architectures can be an effective way to address adhesion issues. Coatings exhibiting excellent tribological properties and durability have been applied on conventionally fabricated Al alloys in the form of duplex systems [36–39] or by inserting transition graded [40–42] and/or element-doped [43,44] layers as the intermediate support for a DLC top film, aiming to alleviate the mismatch in the thermophysical properties and add functionalities to the coating. Trying to replicate these results on SLM Al alloys is still uncharted territory.

The deposition of functional coatings on SLM materials entails further difficulties. A peculiar defect of SLM parts is the poor surface finish, meaning mean surface roughness values of several microns [45–47], which is not only unsuitable for most tribological contacts, but also detrimental for any thin-film deposition process. Post-treatments aimed at reducing surface roughness are thus unavoidable, but their impact on the production effort must be limited, in order to preserve the economic advantages of additive technologies. A previous work by the authors [48] showed that DLC films can be successfully grown at a laboratory scale on SLM AlSi10Mg, and stressed the role of surface roughness in determining the optimal tribological response: interestingly, the best results were found for non-mirror polished substrates. As a drawback, the thin interlayer interposed was not able to conform to substrate bending at increasing contact pressure, and some delamination occurrences were observed.

The aim of this work is therefore primarily to verify the possibility of depositing DLC films on an AlSi10Mg alloy built by SLM to confer durable resistance to wear and self-lubricant characteristics to the surfaces of this material, by following a procedure which is compliant with mass production of parts. For this reason, substrates and coatings fabricated and processed with industrial methods are considered. A multilayer coating is adopted, consisting of an electroless nickel-phosphorus (Ni–P) layer as the base for a transition layer, plus a DLC top thin film. The Ni–P interlayer was chosen to improve the adhesion of the hard topcoat on the Al-alloy, as suggested in [37], and to add anti-corrosive functionalities [49–51]. Moreover, the electroless plating method is particularly advantageous for AM parts, since it enables the formation of coatings of uniform thickness even on intricate shapes [52,53]. The attention here is focused on the tribological behavior of the proposed architectures with reference to their surface finish. The performance of this DLC-based coating system onto SLM surfaces is evaluated by comparison with a similar alloy material produced by conventional casting.

2. Experimental

2.1. Substrates and coatings

For the purposes of the present study, DLC-terminated multilayers of two different types were explored in combination with AlSi10Mg substrates, fabricated both by SLM and by a standard foundry technique, i.e. casting followed by Lathe Manufacturing (LM). The AlSi10Mg substrates were provided in the form of thin discs (4.5 cm in diameter), all annealed after fabrication at a temperature of 160 °C for 4 h to remove possible internal tensions.

Different surface finishing techniques were then applied. SLM samples were processed by sandblasting and grinding (abrasive discs of increasing fineness, from P60 to P180) and by tumbling (ceramic particles, 12 h), which are the standard treatments in the industrial facilities of origin, resulting in well-distinct levels of roughness. An internal laboratory lapping procedure was performed onto LM samples, instead, in order to bring their original roughness down to a value included between those two extremes. In detail, LM samples were first sandblasted and then lapped with foils of increasing fineness, from P220 to P4000, and roughened back with a P320 foil.

The discs were subsequently covered with industrially produced multilayers. The first type of multilayer (Multi-a) consisted of i) a Ni–P layer of 25 μm nominal thickness, grown by electroless deposition on the AlSi10Mg substrate, ii) a Cr/WC-C interlayer deposited by Magnetron Sputtering (MS) and iii) a DLC top layer by Plasma Assisted Chemical Vapor Deposition (PA-CVD). During the PA-CVD process, the substrate

reached a max temperature of about 180 °C. The architecture of the second type of multilayer (Multi-b) was nominally identical to the former one with just the addition of a CrN layer between Cr and WC-C, thus giving a Cr/CrN/WC-C interlayer. Though the deposition techniques used for the single layers were the same in both cases, it is worth to note that Multi-a and Multi-b were produced by different suppliers, presumably implementing different deposition parameters (proprietary information). While Multi-a was applied on both SLM and LM substrates, Multi-b was applied to SLM substrates only. In total, five combinations of AlSi10Mg manufacturing techniques / surface treatments / multilayers were explored (2 discs per combination), as outlined in Fig. 1. Samples prepared with the complete coating architecture, which are the main objects of the present investigation, are named according to the substrate manufacturing technique (SLM or LM), the finishing procedure (G: grinding, T: tumbling, L: lapping) and the applied coating (a: Multi-a, b: Multi-b). In addition to them, samples from intermediate steps of the processing sequence, such as uncovered finished substrates (LM-L, SLM-G and SLM-T) and finished substrates covered with Ni–P only, also visible in the diagram, were retained, for comparative purposes and for complementary characterizations. Lastly, a further sample was produced by depositing the Cr/WC-C interlayer and the DLC top layer belonging to Multi-a type architecture directly onto a ground SLM substrate, with no Ni–P buffer layer interposed, as a term of comparison for the adhesion tests.

2.2. Characterization techniques

The 3-D root mean square roughness (S_q) of the samples was assessed by scanning portions of the disc surface with a contact profilometer (KLA Tencor, P-6 Stylus Profiler, 2 µm tip radius, 60° cone angle). Maps were acquired on just one specimen for each category of samples. In particular, three 2.5×2.5 mm^2 wide regions were scanned on each of the selected discs and results were averaged.

The morphology of the DLC top surface and the interfaces between the various layers of the coatings were observed by means of a Scanning Electron Microscope (SEM) coupled with a Focused Ion Beam (FIB) system (FEI Strata DB 235). The thickness of the layers was determined from the images of ion-milled micro-cross sections. Additional SEM micrographs (FEI Nova NanoSEM 450) and energy-dispersive X-ray (EDX) spectroscopy maps (Bruker Quantax-200 EDX microanalysis system with X-Flash 6|10 detector) were acquired on cross-sections prepared by standard metallographic techniques. To this end, samples were cut with a resin-bound Al$_2$O$_3$-based disc in a semi-automatic machine, hot-mounted in phenol resin, ground with SiC papers from P400 to P4000, polished with a colloidal silica suspension, and ultrasonically cleaned in acetone before the observation. The chemical composition of the SLM and LM substrates and of the electroless Ni–P layers was assessed by EDX spectroscopy on the same polished cross-sections. Spectra were acquired at an electron beam acceleration voltage of 15 kV on four randomly-chosen areas on the substrates and three areas on the Ni–P layers, all imaged at 400×.

The hardness and elastic modulus of the DLC top coatings were determined by depth-sensing nano-indentation (NHT^3, Anton-Paar Tri-Tec) onto the surfaces of samples with ground substrate, using a Berkovich indenter under a maximum load of 10 mN (loading/unloading rate 20 mN/min) corresponding to a typical penetration depth of ~200 nm. The load-penetration curves were analyzed according to the Oliver-Pharr method as described in the ISO 14577-1 standard. The indenter was also periodically verified against a fused silica reference, as recommended by the same standard. The results are given as average ± standard deviation.

The Vickers microhardness of the SLM and LM substrates was assessed by a conventional indentation method at a 1 N load; 12 indents were performed on each substrate type. Again, the results are given as average ± standard deviation.

Scratch tests (Micro-Combi Tester, Anton Paar Tri-Tec) were also performed on the SLM-G-b sample and on a sample where the DLC-based coating was deposited directly onto the ground SLM substrate without the Ni–P layer (as mentioned above). The purpose is to ascertain that the Ni–P layer provided the expected increase in the load-carrying capacity of the system. The tests were carried out in accordance with the ISO 20502 standard, operating with linearly increasing load ("progressive mode scratch test") in the range of 0.02 N - 30 N. The scratch length was 6 mm and the scratch speed was 6 mm/min. The indenter was a Rockwell C-type diamond cone with a 120° opening, and ending in a spherical tip with 200 µm radius. A minimum of six indents were performed on each sample. The critical loads for the onset of specific damage mechanisms were identified by optical microscopy at 200× magnification, as specified by the ISO 20502 standard, and the results were reported as average ± standard deviation. In particular, the critical loads for the first chipping of the DLC-based coating along the edges of the scratch track (L_{C2}) and inside the track (L_{C3}), and the load for its continuous delamination were identified. In addition, instrumental recordings of acoustic emission, friction force, total and residual
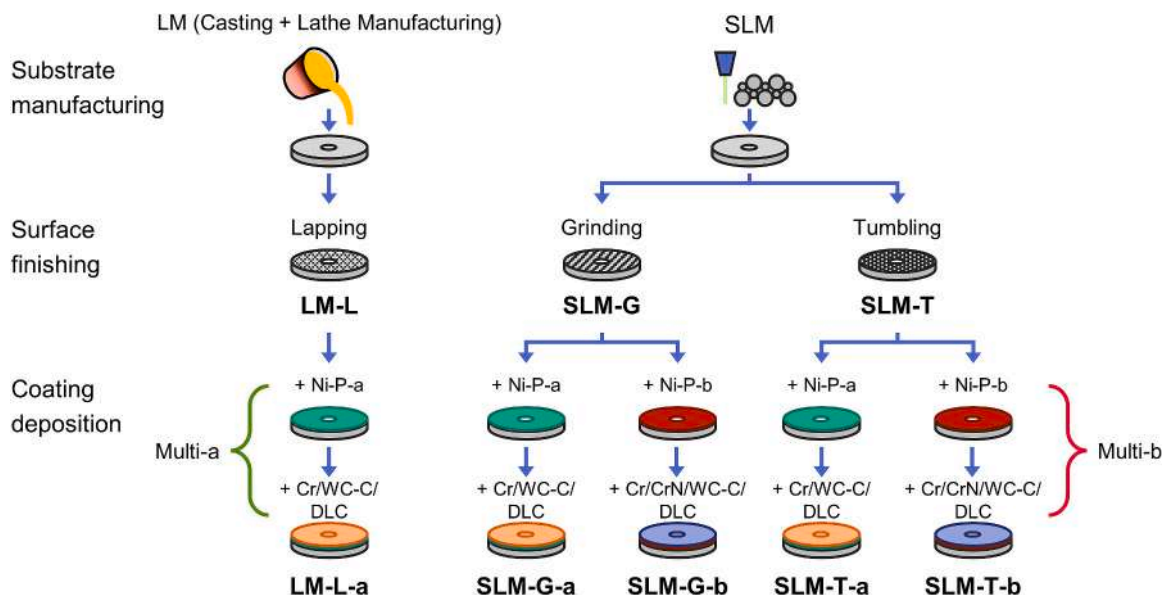

Fig. 1. Diagram of the explored combinations of production techniques. Names highlighted in bold indicate the sample types studied in tribological tests.

penetration depth were acquired to assist in the analysis.

Information on the chemical composition of the DLC coatings was gathered by collecting Raman spectra at multiple positions of the coated discs. A HORIBA Jobin Yvon Raman microscope (LabRAM HR) was adopted, equipped with a Nd-YAG laser source (wavelength 532 nm, 100 mW emission power). The intensity of the laser beam was filtered to 1 % of its emission power to avoid thermal effects. The available wavelength allowed for the detection of just the graphite (G) and the disorder (D) peaks, which are related to carbon bonds (C–C) with sp^2 character. The G peak is due to the bond stretching of all pairs of sp^2 atoms in both rings and chains while the D peak is due to the breathing modes of sp^2 rings as detailed in [54]. Though peaks relative to sp^3 C–C bonding are not discernible, indications on the sp^3-to-sp^2 ratio can be inferred from a deconvolution analysis of the spectra, following the method suggested in [55,56]. At the same time, the bonded H content (C—H) can be extracted from the linear background contribution due to photoluminescence, with the help of the following equation, which was derived in [56] for Raman spectra at 514 nm excitation wavelength:

$$H\ (\%) = 21.7 + 16.6 log[m/I(G)\ (\mu m)]\ \ \ \ \ \ \ \ \ \ \ \ (1)$$

where m is the slope of the background fitting line and I(G) is the intensity of the G peak. Eq. (1) is valid for H contents between 20 % and 50 %.

X-Ray Diffraction (XRD) was applied to evaluate the phase characteristics of the top surface of the AlSi10Mg substrates, Ni–P layers and multilayers. To this aim, a PANalytical X'Pert PRO diffractometer was adopted with the grazing incidence setting, equipped with a Cu X-ray tube operating at 40 mA, 40 kV and a proportional gas detector. The diffraction angle, 2ϑ, was varied between 20° and 85° with a step size of 0.02°. The X'Pert HighScore Plus 2.0 (PANalytical B.V.) software coupled with the ICDD Powder Diffraction File database (PDF-2) was used for phase identification.

Further details on the above-listed characterization techniques, implemented settings and data extraction can be found in [48].

Sliding wear tests were carried out using a ball-on-disc tribometer (CSM Instruments). Normal loads of 1 and 10 N were applied at a constant sliding speed of 100 mm/s in humid air (50–60 % RH) at room temperature (20–24 °C). 100Cr6 balls with a 2D average roughness (R_a) of 0.04 μm and a diameter of 6 mm were adopted as the counterpart, generating initial maximum contact pressures of 0.6 and 1.3 GPa for the loads of 1 N and 10 N, respectively. Two-three tests per applied load were performed on each coated disc (1150 revolutions, sufficient for stabilizing the friction curve) and on bare substrates as well (115 revolutions, in the light of the lower wear resistance of the substrates, which rapidly developed deep grooves), by changing the track radius. Two discs per coating configuration and substrate type were employed. Average friction coefficients (CoFs) and the corresponding standard deviations were computed for each track, by discarding the first 5 % of the data. The weighted average of the results from the same load condition on both samples of the same category was computed. Extended tests (11500 revolutions) were also performed under a load of 10 N on coated samples only (1 track per sample type), in order to reveal any possible variation in the tribological behavior due to prolonged sliding.

Specific wear rates were estimated from the analysis of the wear tracks on the discs and the counterparts. Concerning the disc surfaces, linear profiles were acquired at four cardinal points on each track. The average cross-sectional area of the track (A) was thus extracted and inserted in the following formula:

$$k = \frac{2\pi r A}{L\,l} = \frac{A}{L\,N}\ \ \ \ \ \ \ \ \ \ \ \ (2)$$

where k is the specific wear rate of the sample, r is the track radius, L is the applied load, and l is the distance covered during the entire test, i.e. $2\pi r N$ (being N the number of revolutions). The specific wear rate of the counterpart (k_{ball}), instead, was calculated as:

$$k_{ball} = \frac{V_{ball}}{L\,l} = \frac{\pi h^2(R - h/3)}{L\,l}\ \ \ \ \ \ \ \ \ \ \ \ (3)$$

where R is the ball radius and V_{ball} the ball worn volume, which was assumed to be equal to a spherical cap of height h. The value of h was derived from the area of the ball wear scar, measured from optical microscope images. Also for the specific wear rate, the weighted averages of the results from repeated tests were computed. Wear tracks were also inspected using an Environmental-SEM (FEI Quanta-200) equipped with an Energy Dispersive X-ray (EDX) spectrometer (Oxford INCA-350) for microanalysis.

A summary of the properties investigated for each type of sample is presented in Table 1.

3. Results and discussion

3.1. Topography and morphology of the samples

The microstructure of the SLM and the cast (LM) substrates is notably different in terms of features' size, as shown in Fig. 2. Namely, in both cases the microstructure consists of cellular α-Al grains surrounded by eutectic Si precipitates. In the SLM samples the α-Al grains have a size of approximately 1 to 2 μm, with sub-micrometric Si particles (Fig. 2b). In the LM sample, by contrast, the much lower cooling rate resulted in cellular grains which are 100 times larger (~100–200 μm), with correspondingly coarser Si particles (Fig. 2a). In addition, a few bright inclusions appear in the LM sample (Fig. 2a), which are absent in the SLM sample. Quantitative EDX analyses (Table 2) accordingly show that the LM sample contains small amounts of Fe and Mn, and it also has a slightly higher content of Si. These differences likely stem from the use of different raw materials.

3D maps of the samples are displayed in Fig. S1 of the Supplementary File, relative to the three categories of substrates after surface finishing and the five categories of coated discs. The associated roughness values are summarized in Table 3a and b, respectively. Ground SLM substrates exhibit the lowest S_q, which rises by a factor of three in tumbled samples. As expected, the manual lapping procedure applied to the cast substrates results in an intermediate roughness value. Further differences arise after coating deposition: while the b-type multilayer leaves the initial S_q almost unaffected, a noticeable S_q increment is observed in samples coated with the a-type multilayer, up to values of 3.0 μm and larger. Such opposing results are attributable to differences in the deposition parameters adopted for the two multilayers, especially concerning the nickel plating, as arguable from the comparison of Ni–P covered substrates reported in the Supplementary File. SEM images and 3D maps shown in Fig. S2, as well as the associated roughness data (Table SI) reveal two distinct topographies for the two types of Ni–P, the underlying substrate being equal in terms of manufacturing technique and finishing procedure.

Table 1
Summary of the properties investigated for each type of sample.

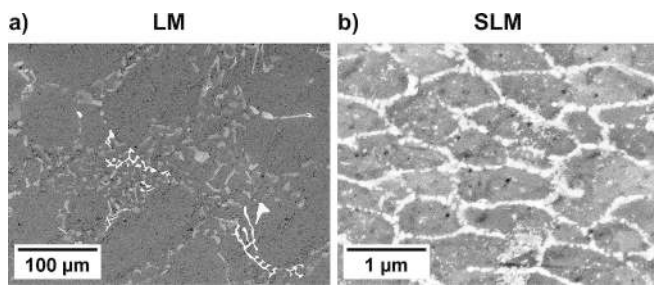|	Coated samples			Bare substrates
Property	Multilayer architecture	Ni-P only	DLC only	
Morphology / Microstr.	X	X		X
Topography	X	X		X
Chemical composition	X	X		X
Crystalline phases	X	X		X
Hardness and elasticity	X	X		X
Adhesion	X		X	
Tribological properties	X			X

Fig. 2. SEM micrographs of metallographic cross-sections of (a) cast (LM) and (b) SLM substrates. Please note the different scales.

Table 2
Chemical composition of cast (LM) and SLM substrates.

Sample	Content (wt%)				
	Mg	Al	Si	Mn	Fe
LM substrate	0.24 ± 0.07	85.70 ± 0.19	13.33 ± 0.14	0.36 ± 0.12	0.33 ± 0.17
SLM substrate	0.26 ± 0.04	90.43 ± 0.03	9.30 ± 0.02	–	–

Table 3
Root mean square roughness of the explored sample categories: (a) bare substrates and (b) coated discs.

	(a) Bare substrates		
	SLM-G	SLM-T	LM-L
S_q (µm)	0.58 ± 0.02	1.8 ± 0.2	1.1 ± 0.1

	(b) Coated discs				
	SLM-G-a	SLM-T-a	LM-L-a	SLM-G-b	SLM-T-b
S_q (µm)	3.0 ± 0.2	3.27 ± 0.05	4.6 ± 0.5	0.47 ± 0.05	1.98 ± 0.10

Fig. 3 displays SEM images of FIB cross sections obtained on the two multilayers. In both the architectures, the deposited layers appear uniform with no evident features. In Multi-a, a DLC film of 2.2 µm in thickness is present above a 1.5 µm thick WC-C/Cr interlayer. Multi-b is globally thinner, the DLC film and the WC-C/Cr/CrN interlayer measuring 1.5 and 1.2 µm, respectively. EDX maps in Fig. S3 (Supplementary File), acquired on metallographic cross sections of the coatings, confirm the composition and stratification of the different layers.

Furthermore, EDX spectra indicate that the P contents of the Ni–P layers in the Multi-a and Multi-b architectures are identical: (10.73 ± 0.11) wt% and (10.46 ± 0.02) wt%, respectively. This means that, despite the different roughness, both of these layers consist of a rather typical kind of high-phosphorus electroless nickel deposition [53].
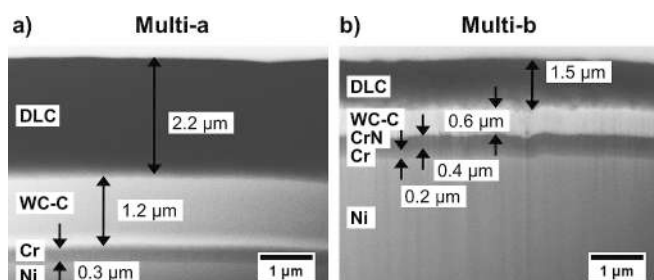

Fig. 3. FIB cross sections of (a) Multi-a and (b) Multi-b coatings.

3.2. Chemical and mechanical characterization

Typical Raman spectra from the DLC top layer on both multilayer types are displayed in Fig. 4a. In order to identify the H content and the sp^2-to-sp^3 ratio, each spectrum is decomposed into three contributions: the background, the D peak and the G peak, fitted by a linear equation, a Lorenzian curve and a Gaussian curve, respectively. Data extracted from the fitting procedure are listed in Table 4: namely, the intensity ratio between the D and the G peak (I(D)/I(G)), the position of the G peak (G-position), and the hydrogen concentration (H(%)). The latter was computed according to Eq. (1). The results indicate that the DLC films are very similar in their bonding structure, irrespective of the substrate fabrication method and the finishing technique, and exhibit only a modest difference in the position of the G peak between the two multilayer types. The numerical values associated to the G-position, together with the measured H content (23–26 %), allow to determine an sp^3 content of nearly 40–45 % for the DLCs under investigation, according to the three-stage model proposed in [55] for a:C-H films.

The XRD patterns of the two multilayers and the substrates are shown in Fig. 4b. In the SLM and LM substrates only aluminum (s.g. Fm-3m, PDF: 00-004-0787) and silicon (s.g. Fd-3m, PDF: 00-027-1402) phases can be identified. The sharp peaks indicate that both samples have a comparable, high degree of crystallinity, with just a different preferential orientation of the crystals, as proven by the change in the relative intensity of the peaks at 2θ = 35.8° and 44.8°.

The XRD patterns of the two coatings (Multi-a and Multi-b) do not show any carbon phases, confirming that DLC coatings are amorphous. The only XRD signals come from the interlayers, whose peculiar structure, both in terms of composition and thickness, gives rise to two slightly different spectra. The Multi-b pattern shows a strong and narrow signal at 35.8° and less intense peaks at 41.6, 60.3, 72.6, and 76.5° attributable to the WC_{1-x} phase (s.g. Fm-3m, PDF: 00-020-1316) contained in the WC-C layer. In addition, two low intensity signals placed at 37.1° and 44.0° are attributable to CrN (s.g. Fm-3m, PDF: 03-065-2899) and Cr (s.g. Im-3m, PDF: 01-085-1336) respectively. The Multi-a pattern shows only one peak attributable to WC-C, at approximately 36.5°, whose large width indicates a lower crystallinity compared to Multi-b. Furthermore, three Cr peaks are detectable at 44, 64.5 and 81.5° respectively. The first intense Cr peak is superimposed on a broad structure embracing an additional WC-C structure and a residual Ni signal (s.g. Fm-3m, PDF: 01-088-2326) that comes from the underlying Ni–P layer, as evident from the Ni–P XRD patterns in Fig. S4.

Depth sensing nano-indentation tests return an elastic modulus (E_{IT}) and a hardness (H_{IT}) of 160 ± 40 GPa and 20 ± 6 GPa, respectively, for the Multi-b system. Since the maximum penetration depth of 200 nm is <20 % of the thickness of the DLC top layer, these values can be regarded as being mostly representative of the properties of the latter. In Multi-a coatings, no meaningful results can be extracted with this method, because of the large surface roughness of the samples. The S_q value of SLM-G-a, which is the lowest in the Multi-a category, is around 6 times higher than that of the corresponding Multi-b coating, i.e. SLM-G-b (Table 3). Consequently, the maximum penetration depth that would be needed with the Multi-a samples would be too large to obtain a value representative of the DLC top layer alone. Nevertheless, since the two types of coatings have a nearly identical contents of H and sp^3, which control the DLC mechanical properties, their E_{IT} and H_{IT} can be reasonably considered equivalent.

The hardness of the AlSi10Mg substrates is notably lower than that of the DLC top layer. Specifically, the LM sample, characterized by a coarser microstructure as shown in Section 3.1, has a Vickers microhardness value of (80 ± 12) HV_{1N}. The comparatively finer and more homogeneous SLM sample has higher average Vicker microhardness with a correspondingly smaller standard deviation: (96 ± 5) HV_{1N}. These values are consistent with the literature, where hardness between 0.8 and 1.4 GPa is reported for AlSi10Mg obtained by casting and SLM manufacturing techniques [12,13,18,20,48].
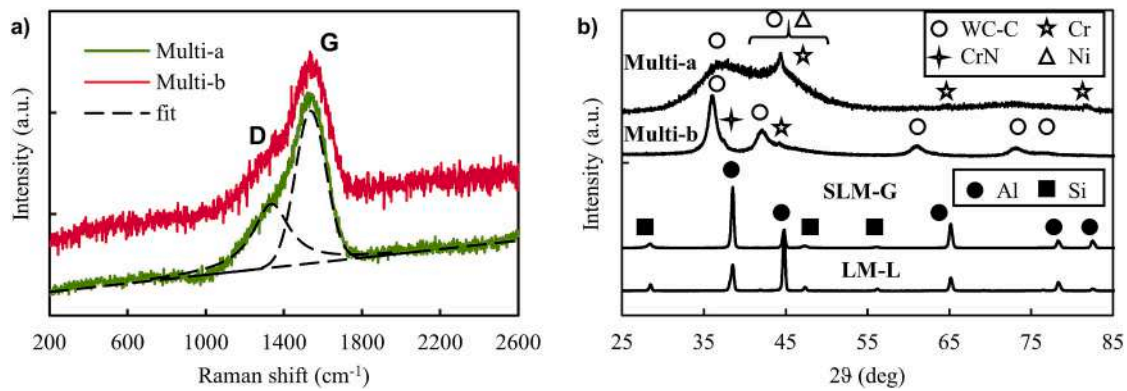
Fig. 4. (a) Raman spectra of the two multilayers. Fits of the D- and G-peak and of the background are presented for exemplificative purposes only for Multi-a. (b) XRD patterns of both the multilayers and the bare substrates (only LM-L and SLM-G samples are shown).

Table 4
Raman parameters and H content of the DLC coatings.

Sample name	I(D)/I(G)	G-position (cm^{-1})	H content (%)
SLM-G-a	0.44 ± 0.05	1544 ± 4	25 ± 2
SLM-T-a	0.41 ± 0.02	1541.3 ± 1.4	26 ± 2
LM-L-a	0.41 ± 0.02	1543 ± 3	23.6 ± 0.9
SLM-G-b	0.43 ± 0.02	1536.3 ± 1.3	23.1 ± 1.2
SLM-T-b	0.44 ± 0.03	1537 ± 2	23.7 ± 1.0

In both cases, however, the huge difference in hardness with the DLC top layer implies that, as mentioned in the Introduction, the film cannot be deposited directly onto the substrate. To confirm this, scratch tests were performed on the SLM-G-b sample and on a ground SLM substrate directly coated with the DLC-based system without any Ni–P interlayer, as described in Section 2.2. The results, listed in Table 5, show that the DLC film deposited directly onto the ground SLM substrate starts to chip along the track edges (L$_{C2}$) at around 10 N, and is entirely delaminated soon after, at a relatively low load of around 15 N. This is also visible in the optical image of a scratch track shown in Fig. 5. The instrumental outputs correspondingly show the abrupt onset of acoustic emission at L$_{C2}$ and a peak emission around the delamination event, accompanied by a sudden increase in the friction coefficient as the diamond indenter starts sliding against the soft, uncovered metal, and in the total and penetration depth values. By contrast, the film deposited onto the Ni–P layer starts to chip (simultaneously along the edge and inside the track) at 12 N and it never delaminates up to the maximum applied load of 30 N. Correspondingly, the instrumental recordings of the friction coefficient and the penetration and residual depths become unstable after the L$_{C3}$ critical load, due to the intermittent chipping of the top layer, but they never show a permanent increase as in the previous case. The different behavior is ascribed to the extensive plastic deformation of the soft AlSi10Mg substrate, which causes substantial stress concentration in the stiff, hard DLC-based film and promotes its removal [57]. The Ni–P interlayer has higher hardness, as measured by depth-sensing nano-indentation (Supplementary File, Table SI), thus providing better mechanical support and a smoother transition from the film to the AlSi10Mg substrate. For this reason, the tribological tests reported in Section 3.3 were performed only on systems with the Ni–P interlayer, as

Table 5
Critical loads for the first chipping of the coating (L$_{C2}$: along the track edges, L$_{C3}$: inside the track) and for its continuous delamination.

Sample	L$_{C2}$ (N)	L$_{C3}$ (N)	Delamination load (N)
SLM-G-b (with Ni–P)	$=$ L$_{C3}$	12.0 ± 1.5	–
SLM substr. + DLC (w/o Ni–P)	10.2 ± 1.2	12.2 ± 1.6	15.0 ± 0.9

described in Section 2.2.

3.3. Tribological results

From the tribological point of view, all the samples coated with the multilayer architectures exhibit similar behaviors. This is illustrated by the curves in Fig. 6, which exemplify the corresponding temporal evolution of the CoF during sliding wear tests at 1 N (Fig. 6a) and 10 N (Fig. 6b). For better clarity, only few cases are reported, which are representative of all the explored combinations of substrate-surface treatment-multilayer. Under a load of 1 N, the multilayer deposited on the cast substrate (sample LM-L-a) shows the typical CoF trend of a-C:H films in humid air, characterized by a peak in the first stages of sliding (occupying nearly 100 revolutions) and by the subsequent stabilization at low values (CoF = 0.20). Such a behavior reflects the activation after some cycles of the self-lubricating properties of DLC, with the possible formation of a carbonaceous transfer layer on the counterpart and the onset of weak chemical bonds between the mating surfaces [58]. Remarkably, the deposited coating architecture allows the DLC film to preserve good frictional performances despite the large surface roughness of the top layer (S$_q$ = 4.6 μm). Such a large roughness is perceived only as noise in the CoF curve. The observed trend is replicated almost identically also in the coated SLM substrates, independently of the multilayer type. A different running-in mechanism seems to occur in Multi-b coating, but with no relevant impact on the subsequent frictional behavior. Raman spectra collected on the wear scar of the counterpart at the end of the tests, such as those presented in Fig. 7 for the tests against sample SLM-G-b, indicate the actual presence of a carbonaceous amorphous transfer film, revealed by the broad structures centered in the carbon's D and G peak region. The intensity variation of such structures at different acquisition points signifies the coverage is not uniform, yet sufficient to facilitate sliding.

When increasing load from 1 to 10 N, the CoF curves slightly shift towards lower values. Such a tendency becomes more evident when plotting the mean values of CoF, reported in Fig. 8. The results from the tests on the coated samples (Fig. 8a) at 1 N are distributed within the range 0.18–0.22. The Multi-a coatings offer a slightly narrower range of CoF mean values as compared to the Multi-b coatings, whose CoF rises from 0.18 to 0.22 if tumbling is applied to the substrates instead of grinding. In the Multi-a coatings, any possible direct influence of the substrate fabrication/preparation technique on friction is concealed by the bigger roughness of the upper layers, induced, probably, by the nickel plating step, as discussed in Paragraph 3.1. Anyway, the differences in the mean CoF between the five groups of samples are within the error range in the majority of cases, with no apparent correlation with the surface roughness. At 10 N, the spread of the mean CoF values is further reduced and spans the range 0.156–0.169. As an additional effect of the higher load, noise in the CoF curves is dampened, indicating a
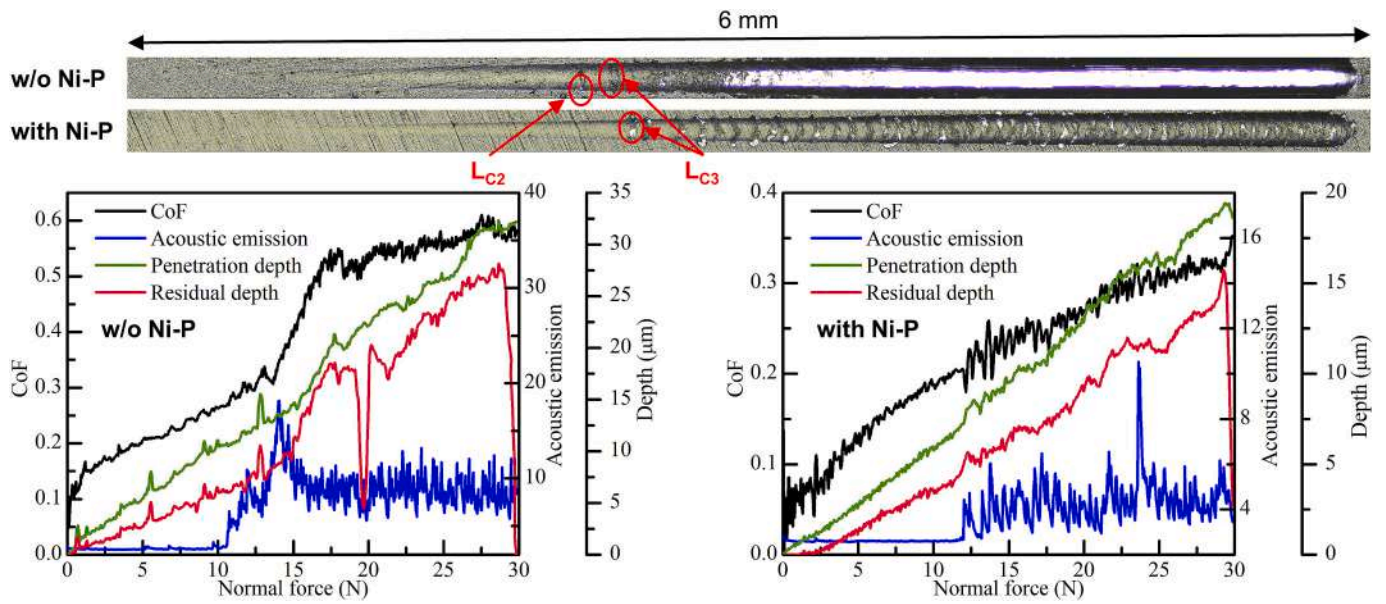
Fig. 5. Optical images of the scratch tracks and instrumental outputs relative to scratch adhesion tests on coated samples with (SLM-G-b) and without Ni–P layer interposed. Please note the change in scale between the plots on the right and those on the left.
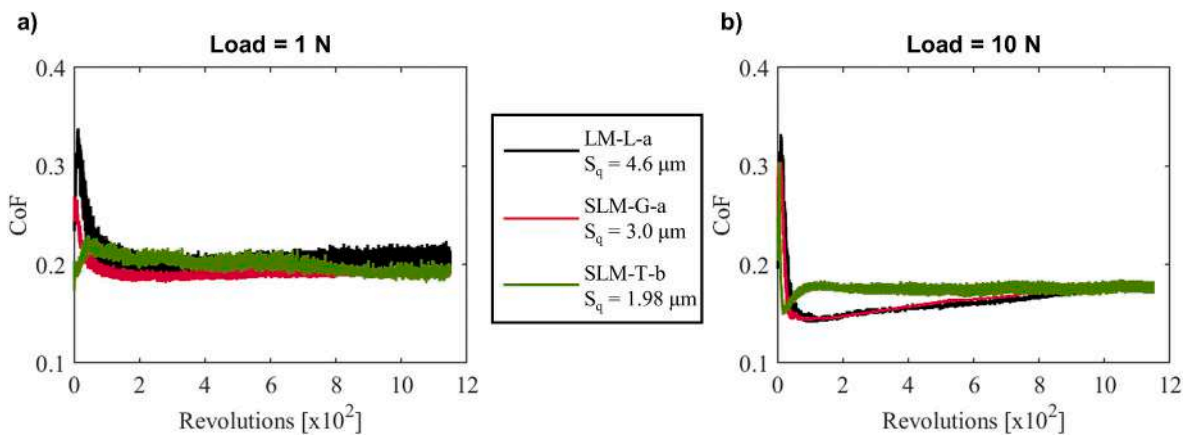

Fig. 6. Evolution of the friction coefficient (CoF) during sliding wear tests at (a) 1 N and (b) 10 N for some representative cases relative to coated samples.
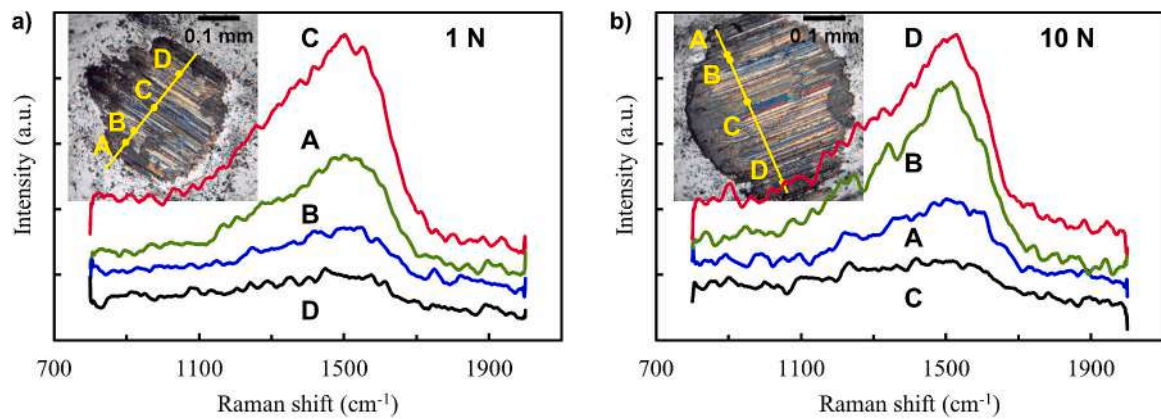

Fig. 7. Raman spectra acquired at multiple points (A–D) on the scar area of the counterpart (shown in the insets) after sliding wear tests at (a) 1 N and (b) 10 N against sample SLM-G-b.
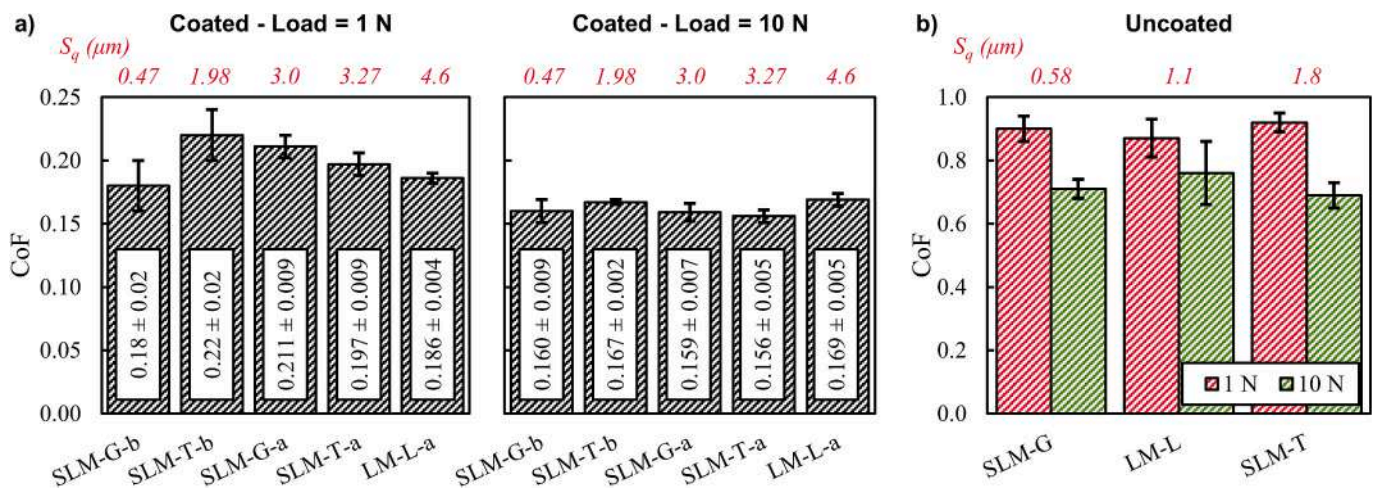
Fig. 8. Average friction coefficients from repeated tests at 1 N and 10 N on (a) coated samples and (b) bare substrates. Please note the change in the y-axis scale between the two panels.

more stable contact with associated more accurate results.

The decrease in CoF with increased loading was already noticed with hydrogen-containing DLC films in other works, where it was ascribed to an enhanced graphitization of the coating [59,60], transfer layer [59,61] and wear debris [62], implying lower friction forces. However, no obvious changes in the structure of carbon atoms consequent to the increase in load can be detected from the current Raman measurements, on either the counterpart wear scars (Fig. 7), or the disc wear tracks (Fig. S5). Furthermore, even with the uncoated discs (Fig. 8b), the CoF at the load of 10 N is once again lower than the value at 1 N, suggesting that graphitization plays a secondary role in determining the CoF variation with load under the present conditions. In general, Multi-a and Multi-b coatings provide far better frictional properties than the bare substrates, whose CoFs are 4–5 times larger, going from 0.69 ± 0.04 to 0.92 ± 0.03, in line with data reported in other studies [48,63]. At the same time, the same 1 N-to-10 N CoF ratios obtained for the multilayers (between 1.10 and 1.33) was also found for the bare substrates, as noted above. This common variation instills the doubt that the linear relationship between the real contact area and the load, predicted by the most popular contact theories for rough surfaces [64,65], is not fulfilled here, so that the friction coefficient, computed as

$$CoF = F_f/L = \tau A_r/L \qquad (4)$$

still preserves a dependence on load. In Eq. (4), F_f is the friction force, τ the shear stress and A_r the real contact area. As an example, the Persson's model [66], which takes into account the elastic coupling between deforming asperities, effectively predicts a deviation from the proportionality between A_r and L when the applied load is sufficiently high. Trying to model the present problem with the existing contact theories is beyond the scope of the present study also for the limited range of tested loads. We limit ourselves to observe that the dependence of the real contact area on load can be simply represented here as $A_r \propto L^{1-x}$, with $0 < x < 1$. Thus, from Eq. (4) we have that $CoF \propto L^{-x}$, from which relation x can be extracted as

$$x = log_{10}\left(\frac{CoF_{1N}}{CoF_{10N}}\right) \qquad (5)$$

By using data in Fig. 8a and b, values of x falling in the range 0.04–0.12 are computed. A possible explanation of this result may reside in the elastic bending of the metallic materials (the Al alloy, and the Ni–P interlayer in the coated systems) under load. Namely, part of the contact stress is relieved by macro-scale elastic bending and, therefore, micro-scale asperities deformation does not increase proportionally with the applied load, resulting in a lower friction coefficient at 10 N. Despite

these bending effects, coating delamination is not observed in these samples, differently from [48], thanks to the presence of the nickel interlayer. Nano-indentation data specified in Table SI prove that Ni–P elasticity is comparable to the DLC one, while its hardness, as noted in Section 3.2, is intermediate between the value measured for the DLC film and the AlSi10Mg substrates. Furthermore, for the present systems the Hertz theory predicts the maximum shear stress to be located within the Ni–P layer under the applied load of 1 N, or slightly below this layer under the maximum applied load of 10 N, instead of being deep in the AlSi10Mg substrate. Thus, the influence of the AlSi10Mg substrate on the ball-on-disc response is limited. The amount of macro-scale elastic bending that the substrate would cause to the DLC film without the Ni–P interlayer would therefore be such that the elastic stress in the film itself would lead to cracking and delamination. The interposed Ni–P layer does not prevent elastic bending entirely (as testified by the lower friction coefficient at 10 N as mentioned above), but it alleviates this effect and improves the adhesion of the coating system.

With bare substrates, the high CoFs are accompanied by a large wear of the surface, with specific wear rates (k) of the order of 10^{-2} mm^3/ (N·m). On the contrary, wear tracks on the coated discs are scarcely detectable, especially on Multi-b coatings. The related SEM micrographs in Fig. S6, panels (b) (Supplementary File), only show sparse bright spots from backscattered electrons, which can be reasonably attributed to a local wear of the coating. This is confirmed by EDX spectra (Fig. S6, panels (a)). In general, apparently undamaged wear track regions produce signals which are identical to those from the surrounding pristine surface. After the tests at 10 N, a decrease in the C and W peaks is notable inside the spots, and Cr peaks appear. It can be deduced that the uppermost layers of the coating, i.e. the DLC and the WC-C film, have been locally consumed, enabling the detection of signals from the underlying elements. In sample SLM-T-b, Fe peaks also become visible, signifying sticking of material from the 100Cr6 ball. Also on Multi-a coatings the wear tracks are characterized by bright spots (Fig. S7, panels (b)). Compared to Multi-b, some differences arise in the corresponding EDX spectra (panels (a)), due to the different heights of the layers composing the coating, as shown in Fig. 3. On Multi-a, wear predominantly involves the DLC film, producing an intensification of the W peaks and the occasional appearance of Cr and Ni peaks from deeper levels. Signals from transferred Fe particles are again observable.

By comparing the SEM images in Figs. S6 and S7 it can be seen that the wear tracks become more evident when increasing the sample roughness and the normal load. However, the coating wear rate remains not measurable. The situation is better illustrated in Fig. 9, where details are provided for the surface of SLM-G-a ($S_q = 3.0$ μm) and LM-L-a ($S_q = 4.6$ μm) samples after the tests at 10 N. The magnified views in panels (a)
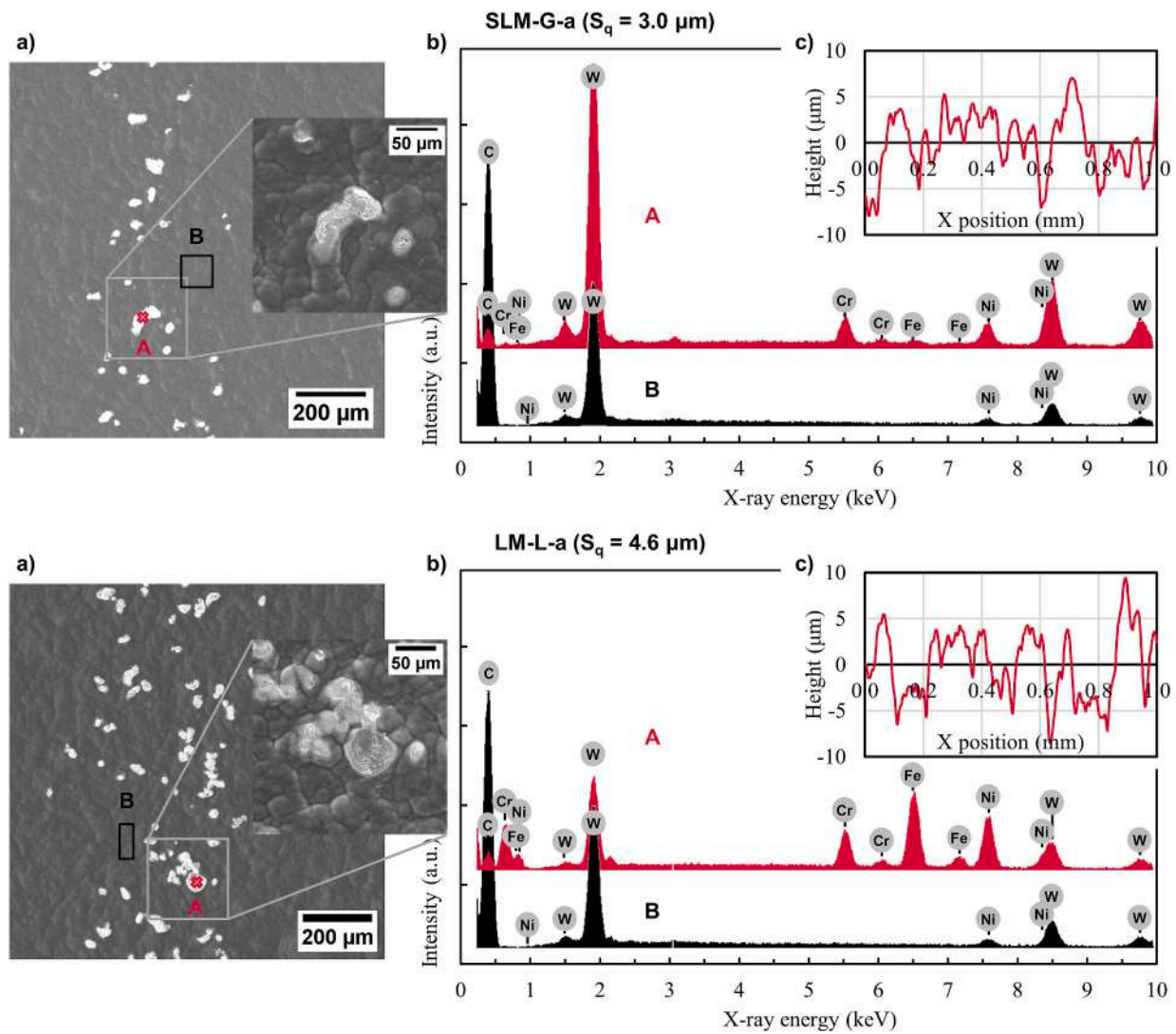
Fig. 9. Wear tracks on samples SLM-G-a and LM-L-a following sliding wear tests at 10 N load (1150 revolutions): (a) SEM images, (b) EDX spectra of zones A and B marked in panel b and (c) 2D profile, centered with respect to the track center line.
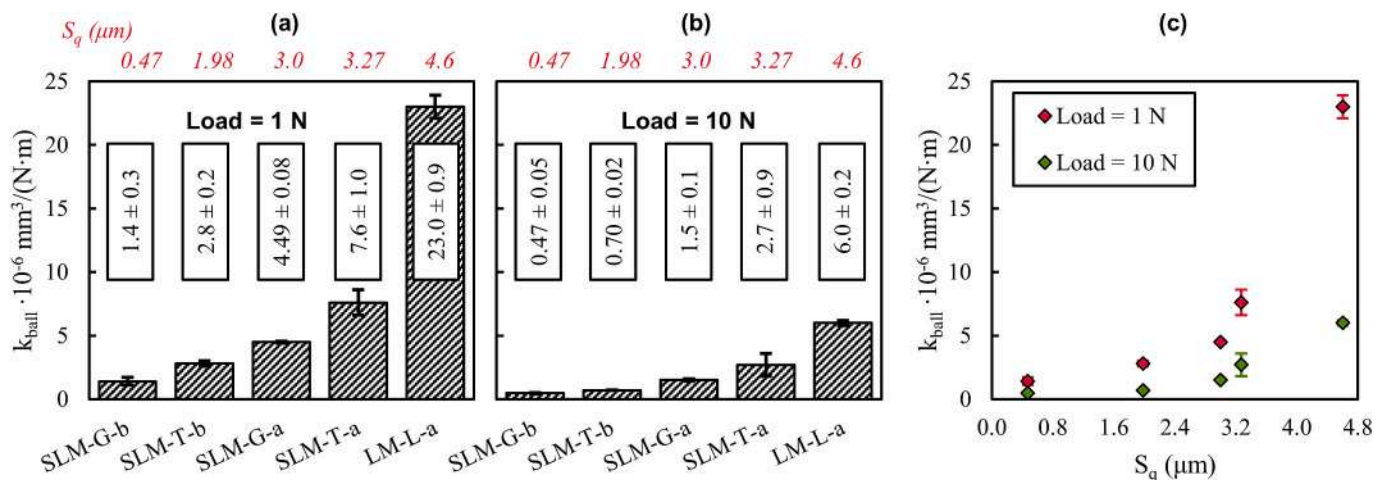

Fig. 10. Specific wear rates of the counterpart from repeated tests on coated samples at (a) 1 N and (b) 10 N (numbers in labels to be multiplied by 10^{-6} mm^3/(N·m)). (c) Plot of the ball wear rate as a function of the coating surface roughness.

show that abrasive wear occurs on the most prominent bulges. As an effect of the larger surface roughness, more asperities come into contact, but even on the roughest sample only the top layers of the coating are involved, as demonstrated by the drop of the carbon signal in EDX spectra from abraded areas in favor of the underlying elements (plus counterpart elements, panels (b)). In some asperities, a consumption of the WC-C layer is found at most, with consequent weakening of the W peaks. Such spotty thinnings of the film do not translate into any significant damage nor into a quantifiable lost volume. Indeed, the track profiles are not distinguishable from the profiles of the surrounding coating surface (panels (c)).

By contrast, a quantitative estimate can be provided for the wear loss of the ball counterpart, by the analysis of optical micrographs of the scar areas like those shown in Figs. S6 and S7, panels (c). The specific wear rates of the ball (k_{ball}) after the tests against the coated samples are plotted in Fig. 10. In tests at 1 N load, k_{ball} values range from 1.4 to 23.0 $\cdot 10^{-6}$ mm^3/(N·m). Consistent with the observations from the SEM images of the disc surfaces, larger wear is found against Multi-a coatings, the cast disc producing the worst results. From the plot in Fig. 10c, it becomes evident that it is the surface roughness of the coatings, rather than any nuance in their composition, which dictates the wear loss of the ball. Indeed, k_{ball} exhibits a clear dependence on S_q, contrary to what was found for the friction coefficient. A possible explanation of this dissimilar behavior may reside in the extent of the abrasive wear occurring during the running-in stage of the tests, which is arguably more considerable with rougher samples because of the larger number of asperities coming into contact. As an effect, a larger wear scar forms on the counterpart when sliding against rougher surfaces, and larger wear tracks are observable, as visible in Figs. S6 and S7. The initial larger wear may also retard the formation of the carbonaceous transfer layer, resulting in a slightly longer duration of the running-in stage, perceivable in Fig. 6. Nonetheless, once developed, the transfer layer allows for the activation of tribo-chemical mechanisms that are not appreciably affected by S_q, producing comparable values of the average CoFs. For all the five combinations, the specific wear rate of the counterpart decreases to nearly 30 % of its value at 1 N when increasing the load to 10 N, qualitatively confirming the trend found for the friction coefficient.

A tenfold extension of the test duration in terms of the number of revolutions leaves the frictional behavior of the coated samples almost unaltered. CoFs measured after 11500 revolutions are consistent with or even smaller than those obtained in the aforementioned tests (1150 revolutions) under the same load (Table 6), indicating that durable, low-friction sliding conditions had already been established in the 1150 revolutions test. Though the wear tracks become larger and more easily recognizable, their profile still blends into the coating roughness, again giving rise to no measurable wear. This is true also in the case of the smoothest sample (SLM-G-b), whose wear tracks at both test durations are compared in Fig. 11a and b. The most relevant result here is not as much the limited consumption of the coatings, which is due to the good mechanical properties of DLC, but rather their resistance to widespread delamination even on SLM substrates prepared via unrefined, industrial-like finishing techniques. The tribological behavior of these systems can be considered comparable to or, as far as wear is concerned, even better than that of coated, conventionally fabricated substrates.

While still limited, the comparatively larger consumption of the coating in the endurance tests may feed the formation of a protective tribo-layer on the counterpart, assisting the preservation of the ball surface. This would justify the decrease in the specific wear rate of the ball which emerges from Table 6, reaching values as low as $5 \cdot 10^{-8}$ mm^3/ (N·m).

4. Conclusions

In this work, DLC-terminated coatings were chosen to improve the tribological performances of the Al–Si alloy AlSi10Mg fabricated by SLM. Two important aspects characterize the novelty of this work, also with reference to the results of a previous study by the authors; namely, the use of a multilayer architecture with the interposition of an electroless Ni–P interlayer between the DLC coating and the Al–Si alloy substrate, and the use of industrial methods to process both substrates and coatings. In particular, two finishing procedures and two slightly different coating structures were evaluated and compared with a similar system grown on a cast substrate. The main outcomes can be summarized as follows.

1) Though Ni–P is frequently employed for its well-known anti-corrosive properties, not investigated here, its mechanical characteristics are also important in regard to the overall load bearing capacity of the coating structure. Scratch tests run on DLC-coated SLM substrates with and without the Ni–P interlayer show that, in the absence of the latter, the film delaminates at a relatively low load, in agreement with already published results. Ni–P interposition helps prevent delamination up to applied scratch loads of at least 30 N.

2) sliding wear tests carried out at two normal loads (1 N and 10 N) reveal that all the five explored combinations of manufacturing technique / finishing procedure / multilayer type produce better frictional performances with respect to the uncoated alloy. The surface roughness of the coating, S_q, spanning the range 0.47–4.6 μm, does not affect the average CoFs, which assume values around 0.20 and 0.16 with the minimum and the maximum load, respectively.

3) Similarly, the specific wear rate of the counterpart decreases when increasing load but, differently from the CoF, it shows a clear dependence on the coating roughness. This dependence was ascribed to more severe abrasive wear occurring during the running-in stage of sliding, due to a greater number of asperities coming into contact with the ball as S_q increases. On the other hand, no appreciable wear of the coating can be measured, and only spotty consumption of the uppermost layers is observable from SEM and EDX analyses of the wear tracks.

4) Raman spectra prove the formation of a carbonaceous transfer layer on the counterpart already at the minimum applied load. Though not uniformly distributed, it accounts for the general good tribological performances observed for the coatings. No evidence of enhanced graphitization is detected, within our experimental limits, when increasing load. The corresponding reduction in CoF could indicate a slightly non-linear dependence of the contact area on the load due to elastic deformation of the Al alloy and the Ni–P layer under load.

The obtained results indicate that DLC-terminated multilayer architectures are extremely efficient on SLM AlSi10Mg components even in the presence of significant roughness. Notably, good tribological performances are obtained by applying well-assessed protocols compatible with large-scale production without the need of additional, time-consuming steps such as mirror finishing to remove surface defects. The studied solution also extends the possible applications of SLM Al–Si alloys, with positive implications for resource savings and fuel economy.

Table 6
Comparison of friction coefficients and ball specific wear rates from repeated sliding wear tests (1150 revolutions) and single endurance tests (11500 revolutions) at 10 N load on the coated samples.

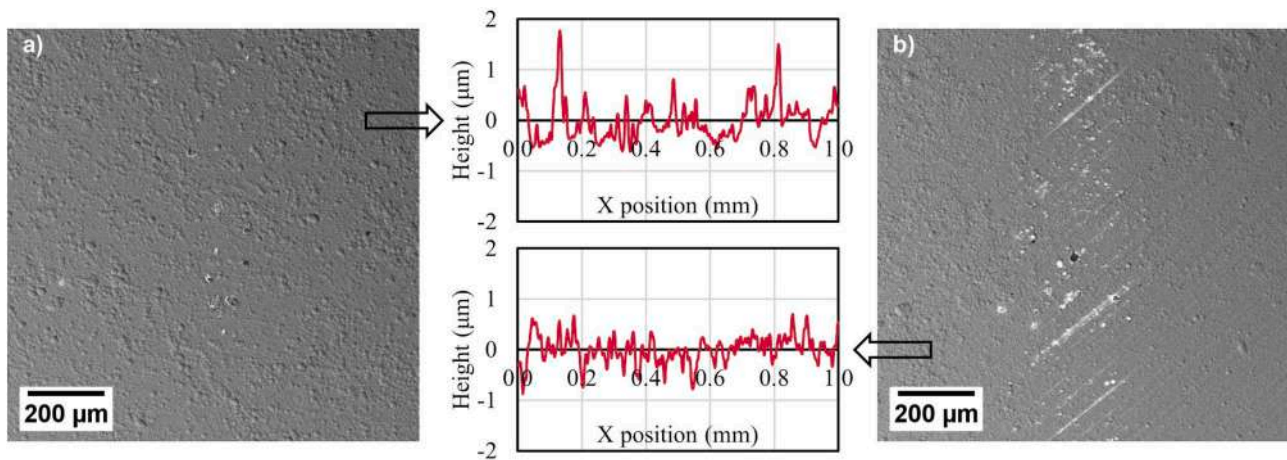| Load: 10 N	CoF		$k_{ball} \cdot 10^{-6}$ mm^3/(N·m)	
Sample	1150 revs.	11500 revs.	1150 revs.	11500 revs.
LM-L-a	0.169 ± 0.005	0.155 ± 0.006	6.0 ± 0.2	1.78 ± 0.06
SLM-G-a	0.159 ± 0.007	0.170 ± 0.005	1.5 ± 0.1	0.22 ± 0.01
SLM-T-a	0.156 ± 0.005	0.153 ± 0.006	2.7 ± 0.9	0.28 ± 0.01
SLM-G-b	0.160 ± 0.009	0.162 ± 0.010	0.47 ± 0.05	0.05 ± 0.01
SLM-T-b	0.167 ± 0.002	0.127 ± 0.005	0.70 ± 0.02	0.23 ± 0.02

Fig. 11. SEM images and 2D profiles of wear tracks on sample SLM-G-b following sliding wear tests at 10 N lasting (a) 1150 and (b) 11500 revolutions. Profiles are centered with respect to the track center line.

CRediT authorship contribution statement

E. Salerno: Writing – review & editing, Writing – original draft, Investigation, Formal analysis, Data curation. **D. Casotti:** Writing – original draft, Investigation, Formal analysis, Data curation. **E. Gualtieri:** Investigation, Data curation. **A. Ballestrazzi:** Investigation, Data curation. **G.C. Gazzadi:** Resources. **G. Bolelli:** Writing – review & editing, Writing – original draft, Investigation. **L. Lusvarghi:** Writing – original draft, Funding acquisition, Conceptualization. **A. Rota:** Writing – review & editing, Writing – original draft, Data curation. **S. Valeri:** Project administration, Funding acquisition, Conceptualization. **G. Paolicelli:** Writing – review & editing, Writing – original draft, Project administration, Conceptualization.

Declaration of competing interest

The authors declare that they have no known competing financial interests or personal relationships that could have appeared to influence the work reported in this paper.

Data availability

Data will be made available on request.

Acknowledgements

Appendix A. Supplementary data

Supplementary data to this article can be found online at https://doi.org/10.1016/j.surfcoat.2024.131422.

References

[1] K.R. Brown, M.S. Venie, R.A. Woods, The increasing use of aluminum in automotive applications, JOM 47 (1995) 20–23, https://doi.org/10.1007/BF03221224.
[2] P.K. Mallick, Overview, in: P.K. Mallick (Ed.), Materials, Design and Manufacturing for Lightweight Vehicles, second ed, Woodhead Publishing, 2021, pp. 1–36, https://doi.org/10.1016/B978-0-12-818712-8.00001-X.
[3] K.K. Sankaran, R.S. Mishra, Aluminum Alloys, in: K.K. Sankaran, R.S. Mishra (Eds.), Metallurgy and Design of Alloys with Hierarchical Microstructures, Elsevier, 2017, pp. 57–156, https://doi.org/10.1016/B978-0-12-812068-2.00004-7.
[4] S.S. Li, X. Yue, Q.Y. Li, H.L. Peng, B.X. Dong, T.S. Liu, H.Y. Yang, J. Fan, S.L. Shu, F. Qiu, Q.C. Jiang, Development and applications of aluminum alloys for aerospace industry, J. Mater. Res. Technol. 27 (2023) 944–983, https://doi.org/10.1016/j.jmrt.2023.09.274.
[5] I.N. Fridlyander, V.G. Sister, O.E. Grushko, V.V. Berstenev, L.M. Sheveleva, L.A. Ivanova, Aluminum alloys: promising materials in the automotive industry, Met. Sci. Heat Treat. 44 (2002) 365–370, https://doi.org/10.1023/A:1021901715578.
[6] A. Graf, Aluminum alloys for lightweight automotive structures, in: P.K. Mallick (Ed.), Materials, Design and Manufacturing for Lightweight Vehicles, second ed, Woodhead Publishing, 2021, pp. 97–123, https://doi.org/10.1016/B978-0-12-818712-8.00003-3.
[7] M. Javidani, D. Larouche, Application of cast Al–Si alloys in internal combustion engine components, Int. Mater. Rev. 59 (2014) 132–158, https://doi.org/10.1179/1743280413Y.0000000027.
[8] A.D. Sarkar, J. Clarke, Wear characteristics, friction and surface topography observed in the dry sliding of as-cast and age-hardening Al-Si alloys, Wear 75 (1982) 71–85, https://doi.org/10.1016/0043-1648(82)90140-5.
[9] M. Elmadagli, T. Perry, A.T. Alpas, A parametric study of the relationship between microstructure and wear resistance of Al-Si alloys, Wear 262 (2007) 79–92, https://doi.org/10.1016/j.wear.2006.03.043.
[10] K. Kanishka, B. Acherjee, Revolutionizing manufacturing: a comprehensive overview of additive manufacturing processes, materials, developments, and challenges, J. Manuf. Process. 107 (2023) 574–619, https://doi.org/10.1016/j.jmapro.2023.10.024.
[11] S.C. Altıparmak, V.A. Yardley, Z. Shi, J. Lin, Challenges in additive manufacturing of high-strength aluminium alloys and current developments in hybrid additive manufacturing, Int. J. Light. Mater. Manuf. 4 (2021) 246–261, https://doi.org/10.1016/j.ijlmm.2020.12.004.
[12] N.T. Aboulkhair, M. Simonelli, L. Parry, I. Ashcroft, C. Tuck, R. Hague, 3D printing of Aluminium alloys: additive manufacturing of Aluminium alloys using selective laser melting, Prog. Mater. Sci. 106 (2019) 100578, https://doi.org/10.1016/j.pmatsci.2019.100578.
[13] J. Zhang, B. Song, Q. Wei, D. Bourell, Y. Shi, A review of selective laser melting of aluminum alloys: processing, microstructure, property and developing trends, J. Mater. Sci. Technol. 35 (2019) 270–284, https://doi.org/10.1016/j.jmst.2018.09.004.
[14] S. Hedge, K.N. Prabhu, Modification of eutectic silicon in Al–Si alloys, J. Mater. Sci. 43 (2008) 3009–3027, https://doi.org/10.1007/s10853-008-2505-5.
[15] I. Rosenthal, A. Stern, N. Frage, Microstructure and mechanical properties of AlSi10Mg parts produced by the laser beam additive manufacturing (AM) technology, Metallogr. Microstruct. Anal. 3 (2014) 448–453, https://doi.org/10.1007/s13632-014-0168-y.
[16] N.E. Uzan, S. Ramati, R. Shneck, N. Frage, O. Yeheskel, On the effect of shot-peening on fatigue resistance of AlSi10Mg specimens fabricated by additive manufacturing using selective laser melting (AM-SLM), Addit. Manuf. 21 (2018) 458–464, https://doi.org/10.1016/j.addma.2018.03.030.
[17] S.I. Shakil, A. Hadadzadeh, B. Shalchi Amirkhiz, H. Pirgazi, M. Mohammadi, M. Haghshenas, Additive manufactured versus cast AlSi10Mg alloy: microstructure and micromechanics, Results Mater. 10 (2021) 100178, https://doi.org/10.1016/j.rinma.2021.100178.
[18] L. Thijs, K. Kempen, J.-P. Kruth, J. Van Humbeeck, Fine-structured aluminium products with controllable texture by selective laser melting of pre-alloyed AlSi10Mg powder, Acta Mater. 61 (2013) 1809–1819, https://doi.org/10.1016/j.actamat.2012.11.052.
[19] K.G. Prashanth, B. Debalina, Z. Wang, P.F. Gostin, A. Gebert, M. Calin, U. Kühn, M. Kamaraj, S. Scudino, J. Eckert, Tribological and corrosion properties of Al-12Si

produced by selective laser melting, J. Mater. Res. 29 (2014) 2044–2054, https://doi.org/10.1557/jmr.2014.133.

[20] M. Lorusso, A. Aversa, D. Manfredi, F. Calignano, E.P. Ambrosio, D. Ugues, M. Pavese, Tribological behavior of aluminum alloy AlSi10Mg-TiB₂ composites produced by direct metal laser sintering (DMLS), J. Mater. Eng. Perform. 25 (2016) 3152–3160, https://doi.org/10.1007/s11665-016-2190-5.

[21] N. Kang, P. Coddet, C. Chen, Y. Wang, H. Liao, C. Coddet, Microstructure and wear behavior of in-situ hypereutectic Al-high Si alloys produced by selective laser melting, Mater. Des. 99 (2016) 120–126, https://doi.org/10.1016/j.matdes.2016.03.053.

[22] V. Vishnu, T.R. Prabhu, K.P. Vineesh, An experimental investigation into the dry reciprocating Wear behavior of additively manufactured AlSi10Mg alloys, JOM 76 (2024) 250–267, https://doi.org/10.1007/s11837-023-06187-6.

[23] R. Hauert, An overview on the tribological behavior of diamond-like carbon in technical and medical applications, Tribol. Int. 37 (2004) 991–1003, https://doi.org/10.1016/j.triboint.2004.07.017.

[24] S.V. Hainsworth, N. Uhure, Diamond-like carbon coatings for tribology applications, Int. Mater. Rev. 52 (2007) 153–174, https://doi.org/10.1179/174328007X160272.

[25] K.A.H. Al Mahmud, M.A. Kalam, H.H. Masjuki, H.M. Mobarak, N.W.M. Zulkifli, An updated overview of diamond-like carbon coating in tribology, Crit. Rev. Solid State and Mater. Sci. 40 (2015) 90–118, https://doi.org/10.1080/10408436.2014.940441.

[26] A. Mescola, A. Lodi, F. Zanni, A. Rota, A. Gerbi, C. Bernini, M. Schott, L. Repetto, A. Camisasca, S. Giordani, R. Buzio, G. Paolicelli, Synergistic effect of graphene and nanodiamonds to achieve ultra-low friction on rough DLC coatings, Diamond Relat. Mater. 145 (2024) 111149, https://doi.org/10.1016/j.diamond.2024.111149.

[27] B. Wielage, A. Dorner, Bonding and sliding wear behaviour of diamond-like carbon coatings on fiber reinforced aluminium, Surf. Coat. Technol. 108-109 (1998) 473–478, https://doi.org/10.1016/S0257-8972(98)00625-2.

[28] A. Grill, Diamond-like carbon: state of the art, Diamond Relat. Mater. 8 (1999) 428–434, https://doi.org/10.1016/S0925-9635(98)00262-3.

[29] C. Donnet, A. Erdemir, Tribology of diamond-like carbon coatings: fundamentals and applications, springer science, N. Y. (2008), https://doi.org/10.1007/978-0-387-49891-1.

[30] S.C. Cha, A. Erdemir, Coating Technology for Vehicle Applications, springer international publishing, Cham (2015), https://doi.org/10.1007/978-3-319-14771-0.

[31] S. Hogmark, S. Jacobson, M. Larsson, U. Wiklund, Mechanical and Tribological requirements and evaluation of coating composites, in: B. Bhushan (Ed.), Modern Tribology Handbook, CRC Press, 2001, pp. 931–964.

[32] R. Wei, P.J. Wilbur, A. Erdemir, F.M. Kustas, The effects of beam energy and substrate temperature on the tribological properties of hard-carbon films on aluminum, Surf. Coat. Technol. 51 (1992) 139–145, https://doi.org/10.1016/0257-8972(92)90228-3.

[33] Y. Sasaki, K. Nose, M. Kamiko, Y. Mitsuda, High adhesion of diamond-like carbon thin film to an aluminum alloy achieved by substrate sputtering and redeposition method, Surf. Coat. Technol. 206 (2011) 143–148, https://doi.org/10.1016/j.surfcoat.2011.07.003.

[34] G.W. Malaczynski, A.H. Hamdi, A.A. Elmoursi, X. Qiu, Diamond-like carbon coating for aluminum 390 alloy-automotive application, Surf. Coat. Technol. 93 (1997) 280–286, https://doi.org/10.1016/S0257-8972(97)00061-3.

[35] G. Bolelli, B. Bonferroni, G. Coletta, L. Lusvarghi, F. Pitacco, Wear and corrosion behaviour of HVOF WC-CoCr/CVD DLC hybrid coating systems deposited onto Aluminium substrate, Surf. Coat. Technol. 205 (2011) 4211–4220, https://doi.org/10.1016/j.surfcoat.2011.03.021.

[36] J.A. Picas, S. Menargues, E. Martina, C. Colominas, M.T. Baile, Characterization of duplex coating system (HVOF + PVD) on light alloy substrates, Surf. Coat. Technol. 318 (2017) 326–331, https://doi.org/10.1016/j.surfcoat.2016.06.020.

[37] M.H. Staia, E.S. Puchi Cabrera, A. Iost, A. Zairi, S. Belayer, A. Van Gorp, Tribological response of AA 2024-T3 aluminium alloy coated with a DLC duplex coating, Tribol. Int. 85 (2015) 74–87, https://doi.org/10.1016/j.triboint.2014.12.007.

[38] X. Nie, A. Leyland, A. Matthews, Deposition of duplex Al₂O₃/DLC coatings on Al alloys for tribological applications using a combined micro-arc oxidation and plasma-immersion ion implantation technique, Surf. Coat. Technol. 121 (2000) 506–513, https://doi.org/10.1016/S0257-8972(00)00816-1.

[39] L. Jin, Y. Li, C. Liu, X. Fan, M. Zhu, Friction mechanism of DLC/MAO wear-resistant coatings with porous surface texture constructed in-situ by micro-arc oxidation, Surf. Coat. Technol. 43 (2023) 130010, https://doi.org/10.1016/j.surfcoat.2023.130010.

[40] L. Wang, S. Wan, S.C. Wang, R.J.K. Wood, Q.J. Xue, Gradient DLC-based nanocomposite coatings as a solution to improve Tribological performance of aluminum alloy, Tribol. Lett. 38 (2010) 155–160, https://doi.org/10.1007/s11249-010-9585-5.

[41] M. Nakamura, S. Kubota, H. Suzuki, T. Haraguchi, Wear and friction characteristics of AlN/diamond-like carbon hybrid coatings on aluminum alloy, J. Mater. Eng. Perform. 24 (2015) 3789–3797, https://doi.org/10.1007/s11665-015-1694-8.

[42] T. Ye, J. Ma, Z. Jia, T. Li, W. Liu, W. Yu, Microstructure, mechanical properties and low-temperature tribological behavior of Cr/Cr-W/W-DLC/DLC multilayer

[43] coatings on 5A06 Al alloy, J. Mater. Res. Technol. 18 (2022) 810–819, https://doi.org/10.1016/j.jmrt.2022.03.002.

[43] H. Maruno, A. Nishimoto, Adhesion and durability of multi-interlayered diamond-like carbon films deposited on aluminum alloy, Surf. Coat. Technol. 354 (2018) 134–144, https://doi.org/10.1016/j.surfcoat.2018.08.094.

[44] H. Cao, X. Ye, H. Li, F. Qi, Q. Wang, X. Ouyang, N. Zhao, B. Liao, Microstructure, mechanical and tribological properties of multilayer Ti-DLC thick films on Al alloys by filtered cathodic vacuum arc technology, Mater. Des. 198 (2021) 109320, https://doi.org/10.1016/j.matdes.2020.109320.

[45] G. Strano, L. Hao, R.M. Everson, K.E. Evans, Surface roughness analysis, modelling and prediction in selective laser melting, J. Mater. Process. Technol. 213 (2013) 589–597, https://doi.org/10.1016/j.jmatprotec.2012.11.011.

[46] A.H. Maamoun, Y.F. Xue, M.A. Elbestawi, S.C. Veldhuis, Effect of selective laser melting process parameters on the quality of Al alloy parts: powder characterization, density, surface roughness, and dimensional accuracy, Materials 11 (2018) 2343, https://doi.org/10.3390/ma11122343.

[47] P. Renner, S. Jha, Y. Chen, A. Raut, S.G. Mehta, H. Liang, A review on corrosion and Wear of additively manufactured alloys, J. Tribol. 143 (2021) 050802, https://doi.org/10.1115/1.4050503.

[48] E. Salerno, D. Casotti, G. Paolicelli, E. Gualtieri, A. Ballestrazzi, G.C. Gazzadi, G. Bolelli, L. Lusvarghi, S. Valeri, A. Rota, Friction and wear of DLC films deposited on additive manufactured AlSi10Mg: the role of surface finishing, Surf. Coat. Technol. 463 (2023) 129531, https://doi.org/10.1016/j.surfcoat.2023.129531.

[49] E.S. Puchi-Cabrera, C. Villalobos-Gutiérrez, I. Irausquín, J. La Barbera-Sosa, G. Mesmacque, Fatigue behavior of a 7075-T6 aluminum alloy coated with an electroless Ni–P deposit, Int. J. Fatigue 28 (2006) 1854–1866, https://doi.org/10.1016/j.ijfatigue.2005.12.005.

[50] W. Qin, Microstructure and corrosion behavior of electroless Ni-P coatings on 6061 aluminum alloys, J. Coat. Technol. Res. 8 (2011) 135–139, https://doi.org/10.1007/s11998-010-9256-3.

[51] N. Sridhar, K.U. Bhat, Effect of deposition time on the morphological features and corrosion resistance of Electroless Ni-high P coatings on Aluminium, J. Mater. 2013 (2013) 985763, https://doi.org/10.1155/2013/985763.

[52] J. Sudagar, J. Lian, W. Sha, Electroless nickel, alloy, composite and nano coatings - a critical review, J. Alloys Compd. 571 (2013) 183–204, https://doi.org/10.1016/j.jallcom.2013.03.107.

[53] W. Sha, X. Wu, K.G. Keong, Electroless Copper and Nickel-Phosphorus Plating, Processing, characterisation and modelling,, Woodhead Publishing Ltd., Cambridge, UK, 2011.

[54] A.C. Ferrari, Determination of bonding in diamond-like carbon by Raman spectroscopy, Diamond Relat. Mater. 11 (2002) 1053–1061, https://doi.org/10.1016/S0925-9635(01)00730-0.

[55] A.C. Ferrari, J. Robertson, Interpretation of Raman spectra of disordered and amorphous carbon, Phys. Rev. B 61 (2000) 14095, https://doi.org/10.1103/PhysRevB.61.14095.

[56] C. Casiraghi, A.C. Ferrari, J. Robertson, Raman spectroscopy of hydrogenated amorphous carbons, Phys. Rev. B 72 (2005) 085401, https://doi.org/10.1103/PhysRevB.72.085401.

[57] C.T. Wang, T.J. Hakala, A. Laukkanen, H. Ronkainen, K. Holmberg, N. Gao, R.J.K. Wood, T.G. Langdon, An investigation into the effect of substrate on the load-bearing capacity of thin hard coatings, J. Mater. Sci. 51 (2016) 4390–4398, https://doi.org/10.1007/s10853-016-9751-8.

[58] H. Ronkainen, K. Holmberg, Environmental and thermal effects on the Tribological performance of DLC coatings, in: C. Donnet, A. Erdemir (Eds.), Tribology of Diamond-Like Carbon Coatings: Fundamentals and Applications, Springer Science, New York, 2008, pp. 155–200.

[59] J. Solis, H. Zhao, C. Wang, J.A. Verduzco, A.S. Bueno, A. Neville, Tribological performance of an H-DLC coating prepared by PECVD, Appl. Surf. Sci. 383 (2016) 222–232, https://doi.org/10.1016/j.apsusc.2016.04.184.

[60] D.W. Kim, K.W. Kim, Effects of sliding velocity and normal load on friction and wear characteristics of multi-layered diamond-like carbon (DLC) coating prepared by reactive sputtering, Wear 297 (2013) 722–730, https://doi.org/10.1016/j.wear.2012.10.009.

[61] Y. Liu, L. Wang, T. Liu, P. Zhang, Effect of normal loads and mating pairs on the tribological properties of diamond-like carbon film, Wear 486-487 (2021) 204083, https://doi.org/10.1016/j.wear.2021.204083.

[62] Y. Liu, A. Erdemir, E.I. Meletis, An investigation of the relationship between graphitization and frictional behavior of DLC coatings, Surf. Coat. Technol. 86-87 (1996) 564–568, https://doi.org/10.1016/S0257-8972(96)03057-5.

[63] V. Mára, J. Krčil, L. Pilsová, Problematic of heat treatment and its influence on mechanical properties of selectively laser melted AlSi10Mg alloy, Int. J. Adv. Manuf. Technol. 119 (2022) 5743–5761, https://doi.org/10.1007/s00170-021-08521-1.

[64] J.A. Greenwood, J.B.P. Williamson, Contact of nominally flat surfaces, Proc. R. Soc. Lond. A 295 (1966) 300–319, https://doi.org/10.1098/rspa.1966.0242.

[65] A.W. Bush, R.D. Gibson, T.R. Thomas, The elastic contact of a rough surface, Wear 35 (1975) 87–111, https://doi.org/10.1016/0043-1648(75)90145-3.

[66] B.N.J. Persson, Contact mechanics for randomly rough surfaces, Surf. Sci. Rep. 61 (2006) 201–227, https://doi.org/10.1016/j.surfrep.2006.04.001.